Monthly Notices of the ROYAL ASTRONOMICAL SOCIETY

MNRAS **542,** L117–L125 (2025) https://doi.org/10.1093/mnrasl/slaf079
Advance Access publication 2025 July 21

JWST reveals cosmic ray dominated chemistry in the local ULIRG IRAS 07251−0248

G. Speranza [1]★ M. Pereira-Santaella,[1] M. Agúndez,[1] E. González-Alfonso,[2] I. García-Bernete [3] J. R. Goicoechea,[1] M. Imanishi [4] D. Rigopoulou [5,6] M. G. Santa-Maria[1,7] and N. Thatte[5]

[1]*Instituto de Física Fundamental, CSIC, Calle Serrano 123, E-28006 Madrid, Spain*
[2]*Departamento de Física y Matemáticas, Universidad de Alcalá, Campus Universitario, E-28871 Alcalá de Henares, Spain*
[3]*Centro de Astrobiología (CAB), CSIC-INTA, Camino Bajo del Castillo s/n, E-28692 Villanueva de la Cañada, Spain*
[4]*National Astronomical Observatory of Japan, 2-21-1 Osawa, Mitaka, Tokyo 181-8588, Japan*
[5]*Department of Physics, University of Oxford, Keble Road, Oxford OX1 3RH, UK*
[6]*School of Sciences, European University Cyprus, Diogenes street, Engomi, 1516 Nicosia, Cyprus*
[7]*Department of Astronomy, University of Florida, P.O. Box 112055, Gainesville, FL 32611, USA*

Accepted 2025 July 17. Received 2025 July 16; in original form 2025 May 6

ABSTRACT

We analyse the ro-vibrational absorption bands of various molecular cations (HCO^+, $HCNH^+$, and N_2H^+) and neutral species (HCN, HNC, and HC_3N) detected in the *James Webb Space Telescope*/Mid-Infrared Instrument Medium Resolution Spectrometer spectrum (4.9–27.9 μm) of the local ultraluminous infrared galaxy IRAS 07251−0248. We find that the molecular absorptions are blueshifted by 160 km s^{-1} relative to the systemic velocity of the target. Using local thermal equilibrium excitation models, we derive rotational temperatures ($T_{\rm rot}$) from 42 to 185 K for these absorption bands. This range of measured $T_{\rm rot}$ can be explained by infrared radiative pumping as a by-product of the strength, effective critical density, and opacity of each molecular band. Thus, these results suggest that these absorptions originate in a warm expanding gas shell ($\dot{M}\sim$90–330 M$_\odot$ yr^{-1}), which might be the base of the larger scale cold molecular outflow detected in this source. Finally, the elevated abundance of molecular cations can be explained by a high cosmic ray ionization rate, with $\log(\zeta_{H_2}/n_{\rm H}\,[{\rm cm^3\,s^{-1}}])$ in the range of −18.2 (from H_3^+) to −19.1 (inferred from HCO^+ and N_2H^+, which are likely tracing denser gas), consistent with a cosmic ray dominated chemistry as predicted by chemical models.

Key words: ISM: abundances – cosmic rays – ISM: molecules – galaxies: active – galaxies: ISM.

1 INTRODUCTION

Local ultraluminous infrared galaxies (ULIRGs; $L_{\rm IR,\,8–1000\,\mu m} > 10^{12}\,L_\odot$) represent a crucial phase in galaxy evolution, as most of them are gas-rich major mergers (e.g. Hung et al. 2014). Their nuclei are deeply embedded in dust-obscured environments, with column densities exceeding $N_{\rm H} > 10^{24}$ cm^{-2} (e.g. González-Alfonso et al. 2015; Falstad et al. 2021; García-Bernete et al. 2022a; Donnan et al. 2023). In such extreme conditions, determining whether the gas primarily fuels active galactic nuclei, intense starbursts (SB), or both remains challenging. To disentangle the dominant excitation mechanisms within ULIRG cores, interstellar molecular gas has been extensively analysed (e.g. Pereira-Santaella et al. 2021; Esposito et al. 2022; Imanishi et al. 2023; Holden et al. 2024). These previous works were mostly based on the observation of molecular rotational transitions of CO, HCN, and HCO^+ in the mm and sub-mm ranges using the Atacama Large Millimeter/submillimeter Array (ALMA) and the Northern Extended Millimetre Array (NOEMA). An alternative view of the molecular content is provided by the ro-vibrational molecular bands in the mid-IR. The strongest molecular bands (CO, HCN, and C_2H_2) have been detected in some galaxies using space (*Spitzer* and *AKARI*) and ground-based observations (e.g. Spoon et al. 2004; Lahuis et al. 2007; Baba et al. 2018; Onishi et al. 2021). Recently, thanks to its superb sensitivity and spatial and spectral resolutions, *James Webb Space Telescope* (*JWST*) has opened a new window for studying the rich chemistry of ULIRGs through molecular bands from less abundant species (e.g. Buiten et al. 2024; González-Alfonso et al. 2024; Pereira-Santaella et al. 2024a; García-Bernete et al. 2024b; Buiten et al. 2025).

In this Letter, we analyse the absorption bands of molecular cations in the rich mid-IR spectrum of the eastern nucleus of the ULIRG IRAS 07251−0248 (hereafter IRAS 07251; $d = 400$ Mpc; $z = 0.0878$; $L_{\rm IR} = 12.45\,L_\odot$; Pereira-Santaella et al. 2021). This nucleus dominates the $L_{\rm IR}$ of the system and host a deeply dust embedded compact core as indicated by the deep 9.7 μm silicate absorption, the strong OH absorptions in the far-IR (González-Alfonso et al. 2017), and a blueshifted CO $J = 2-1$ absorption toward the nuclear 230 GHz continuum (Lamperti et al. 2022).

IRAS 07251 also has one of the highest H_3^+ abundances, derived from the ro-vibrational υ_2 band of H_3^+ in a sample of local ULIRGs, as reported by Pereira-Santaella et al. (2024b) using *JWST*/NIRSpec

★ E-mail: giovanna.speranza@iff.csic.es

observations. Specifically these authors measured $N(H_3^+)/N_H = 4.9 \times 10^{-7}$ for this target, in which the H_3^+ υ_2 band is detected in absorption. H_3^+ is a key molecule in cosmic-ray dominated regions (CRDR), the expected environment for ULIRGs, where UV and X-ray photons are mostly absorbed (e.g. Papadopoulos 2010). We note that, considering the difficulties in detecting H_3^+ before the advent of *JWST*, alternative diagnostics have been studied to estimate the cosmic ray ionization rate (CRIR; see Fontani et al. 2017; Bovino et al. 2020; Redaelli et al. 2024). Observations and theoretical models suggest that CRIR are attenuated when entering dense clouds (e.g. Padovani, Hennebelle & Galli 2013; Socci et al. 2024), but enhanced by the action of shocks, as in protostellar-like environments (e.g. Gaches & Offner 2018; Pineda et al. 2024).

Additionally, H_3^+ initiates the chain of chemical reactions that enrich the interstellar medium (ISM; e.g. Agúndez & Wakelam 2013; Oka 2013). Therefore, molecular cations are expected to be abundant in CRDRs. However, with the notable exception of HCO^+, observations of molecular cations remain primarily limited to Galactic studies. HCO^+ and N_2H^+ have been extensively studied within the Milky Way (e.g. Pety et al. 2017; Agúndez et al. 2019; Fuente et al. 2019; Santa-Maria et al. 2021). Podio et al. (2014) and Ceccarelli et al. (2014) suggested that the HCO^+/N_2H^+ abundance ratio decreases with increasing CRIR, but the detection of both cations is reported in only a few extragalactic studies (e.g. Meier & Turner 2012; Jiménez-Donaire et al. 2023). Similarly, $HCNH^+$, which forms via protonation of HCN or HNC, has been observed in only one extragalactic case (Harada et al. 2024). IRAS 07251 therefore represents an ideal target for detecting and characterizing such molecular cations, which remain almost unexplored in extragalactic environments.

We present an analysis of the mid-infrared spectrum of IRAS 07251, observed with the Mid-Infrared Instrument (MIRI; Glasse et al. 2015) using the Medium Resolution Spectrometer (MRS; Wells et al. 2015) onboard *JWST*. MIRI MRS covers the 4.9–27.9 μm range with a resolving power of $R \sim 1300$–3700 (Labiano et al. 2021; Argyriou et al. 2023). This study represents the first attempt to characterize ISM chemistry in an extragalactic source using this molecular suite.

2 ANALYSIS AND RESULTS

The mid-IR spectrum of the eastern nucleus of IRAS 07251 shows absorptions associated with several ro-vibrational bands of neutral molecules and cations. In particular, we investigate the fundamental bands of HCO^+ υ_2, $HCNH^+$ υ_4 and υ_5, N_2H^+ υ_2, HC_3N υ_5, and HNC υ_2 (see Table 1), complemented by the HCN $2\upsilon_2$ and υ_2 bands analysed by García-Bernete et al. submitted. Details on data reduction and the molecular spectroscopic parameters are provided in Appendices A and B, respectively. All measurements are reported in Table 1 and shown in Fig. 1.

We estimated the rotational temperature (T_{rot}) and column density (Table 1) of each vibrational band by fitting the spectra using a local thermal equilibrium (LTE) model. To do so, we first normalized the observed spectra by the local continuum level, estimated through a spline-interpolated baseline. The radiative transfer LTE models assume a background emission source and a homogeneous layer of molecular material in front, whose rotational levels are populated according to a single T_{rot}. For each molecule, we constructed a grid of 50×50 models where the column density, N, and T_{rot} varied. We find that the molecular absorptions are blueshifted by $-160\,km\,s^{-1}$ relative to the rest-frame velocity of this object (based on CO $J = 2$–1; Pereira-Santaella et al. 2021). This suggests that these molecular absorptions are produced in an expanding shell and may represent the innermost part of the molecular outflow reported by Lamperti et al. (2022). We adopted an intrinsic velocity dispersion, σ, of $105\,km\,s^{-1}$ based on the width of non blended molecular lines (see García-Bernete et al. submitted).

Table 1. Molecular absorption bands.

Name(1)	λ (2) [μm]	T_{rot} (3) (K)	N (4) (10^{15} cm^{-2})	N/N_H (5) (10^{-8})	f (6)
HCO^+ υ_2	12.07	42 ± 14	33.9 ± 3.1	18	0.7
$HCNH^+$ υ_4	12.49	172 ± 24	16.3 ± 1.3	8.6	0.7
N_2H^+ υ_2	14.59	48 ± 30	2.1 ± 0.5	1.1	0.7
HC_3N υ_5	15.08	122 ± 60	10.0 ± 0.7	5.3	0.7
$HCNH^+$ υ_5	15.51	152 ± 19	3.6 ± 0.2	1.9	0.7
HNC υ_2	21.61	48 ± 5	55.7 ± 7.4	29	0.14 ± 0.08
HCN[a] $2\upsilon_2$	7.10	185 ± 25	2000 ± 600	1100	0.6
HCN[a] υ_2	14.04	100 ± 25	660 ± 240	350	0.7

Notes. (1) Ro-vibrational band; (2) Rest-frame wavelength of the Q(1) transition, except for HCN $2\upsilon_2$, for which the R(1) transition is reported; (3) Rotational temperature; (4) Column density; (5) Fractional abundance adopting $N_H = 1.89 \times 10^{23}$ cm^{-2} from Pereira-Santaella et al. (2024b); (6) Covering factor.
[a]Values for HCN are from García-Bernete et al. submitted.

We select as best fit model that with the minimum χ^2 between observation and model. For all bands except HNC υ_2, the χ^2 computation was performed only on the spectral range covered by the Q-branch, since the R-branch is only tentatively detected in most bands, and the P-branch is fainter. The line overlap is taken into account in the fitting procedure. Although the individual ro-vibrational transition lines are spectrally unresolved in the Q-branch, the fit is sensitive to the rotational temperature since the Q-branch broadens with increasing rotational temperature as higher J levels are populated. Before the χ^2 evaluation, a covering factor (f) of 0.7 (based on García-Bernete et al. submitted) is applied to all models. The covering factor is defined as the ratio between the absorbed continuum and the total continuum (absorbed plus unabsorbed), which is equivalent to the 'background factor' defined in Buiten et al. (2025). In order to model the Q-branch of N_2H^+ υ_2, we accounted for contamination from the HCN υ_2 P(9) line. To do so, we fitted the HCN υ_2 P(8) and P(10) lines and interpolated the strength of the P(9) line from the T_{rot} determined from the other two P transitions. The model for N_2H^+ υ_2 is then obtained after removing such contribution. For the HNC υ_2 band, both the R and the P branches are clearly detected up to $J_{low} = 8$. Therefore, we computed χ^2 over the full wavelength range (i.e. 20.30–22.85 μm), which includes the R- and P-branches. In this case, f was treated as free parameter of the model, as the contribution from the colder dust continuum becomes more significant at longer wavelengths (e.g. Donnan et al. 2024), leading to a lower fraction of absorbed warm continuum. Indeed, we obtained $f = 0.14 \pm 0.08$ for HNC υ_2 (Table 1).

The parameters of the best-fitting models are listed in Table 1 and shown in Fig. 1. Errors on the measured T_{rot} and N are calculated from a series of 100 Monte Carlo simulations. In the case of N_2H^+, both the total profile and the HCN model have been perturbed to account for the uncertainty due to the line blending. The resulting T_{rot} range from 40 K to 185 K. The $HCNH^+$ υ_4 and υ_5 and HCN $2\upsilon_2$ bands reach the highest temperatures (∼150–185 K), while the rest of cations and neutral molecules exhibit lower T_{rot} between 40 and 120 K.

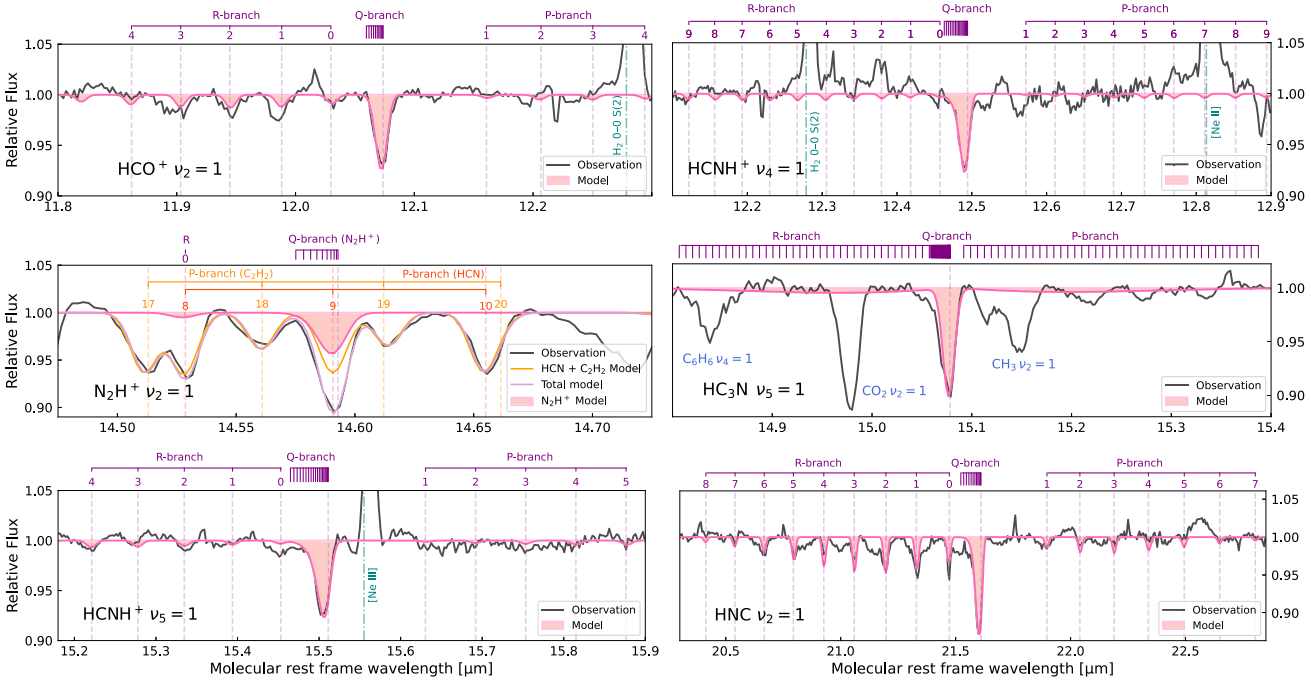

Figure 1. LTE models and continuum-normalized observed spectra of the fundamental ro-vibrational bands detected in absorption: from left to right and top to bottom HCO$^+$ υ_2, HCNH$^+$ υ_4, N_2H^+ υ_2, HC_3N υ_5, HCNH$^+$ υ_5, and HNC υ_2. The observed spectra are shown in black, models are represented by pink line and shaded area. Vertical dashed purple lines indicate the wavelength of the resolved transitions of the P- and R-branches and the origin of the Q-branch. The numbers at the top of each panel indicate the rotational number J of the lower level of the transition. All panels are displayed in the molecular rest frame, which is blueshifted by $\sim 160\,\mathrm{km\,s^{-1}}$ relative to the systemic velocity of this target (based on CO $J = 2$–1; Pereira-Santaella et al. 2021). The wavelengths (in the molecular rest frame) of the detected emission lines are marked by dashed-dotted green lines (H_2 0–0 S(2) at 12.28 μm, [Ne II]λ12.81 μm, and [Ne III]λ15.56 μm). The N_2H^+ panel includes the model of the P(17) to P(20) transitions of C_2H_2 υ_5 and the P(8) to P(10) transitions of HCN υ_2 (dashed orange vertical lines and the orange model). The total model is shown in violet, while the N_2H^+ model is displayed in pink with a shaded area, as the rest of detections.

3 DISCUSSION

3.1 IR radiative pumping to explain the observed $T_{\rm rot}$ range

As shown in Table 1, $T_{\rm rot}$ vary by up to ∼140 K ranging from the lowest temperature measured for HCO$^+$ υ_2 (42 K) to the highest reported for HCNH$^+$ υ_4 (172 K) and HCN $2\upsilon_2$ (185 K). Based on the analysis of the strong molecular bands (HCN, C_2H_2, and H_2O) in this source by González-Alfonso et al. (in preparation), we expect all these bands to originate in a relatively small volume (r < 20–75 pc) close to the compact IR core of IRAS 07251. Therefore, in this section, we investigate if radiative pumping excitation can explain the wide range of observed $T_{\rm rot}$.

Different $T_{\rm rot}$ are expected due to the different responses of each molecule when exposed to an IR radiation field (Einstein B coefficients) and their different collisional excitation rate coefficients (thus, different critical densities). These effects were discussed by Imanishi, Nakanishi & Izumi (2016) to explain the ground state and vibrationally excited HCN/HCO$^+$/HNC $J = 3 - 2$ emissions in the ULIRG IRAS 20551−4250, where IR radiative pumping is the dominant excitation mechanism.

Here, we further explore whether IR radiation can produce the observed $T_{\rm rot}$ for these bands by performing non-local thermodynamic equilibrium (NLTE) models under the large velocity gradient formalism. For these NLTE models, we assume an illuminating blackbody with temperatures ($T_{\rm rad}$) from 200 to 500 K with a dilution equivalent to a cloud located at a distance of 50 pc from a source with a radius of 20 pc, a kinetic temperature ($T_{\rm kin}$) of ∼200 K (based on measurements from González-Alfonso et al. (in preparation) and García-Bernete et al. submitted), and $n_{\rm H_2} = 10^4\mathrm{cm}^{-3}$ as fiducial values. Then, we determined the apparent $T_{\rm rot}$ of the simulated NLTE absorption band by finding the best-fitting model from the LTE grids used in Section 2.

The left panel of Fig. C1 shows the apparent $T_{\rm rot}$ of the NLTE models as a function of $T_{\rm rad}$. The different response of each molecule to the radiation field is clear in this figure. The HCNH$^+$ curve is the closest to $T_{\rm rot} = T_{\rm rad}$ at all $T_{\rm rad}$, whereas HCO$^+$ is the least efficient reacting to the radiation field.

For HCO$^+$ υ_2, its lower trend with respect to the other curves is due to its relatively low Einstein B coefficient, which is the smallest among the studied bands (2 to 13 times lower than the others), excluding HCN $2\upsilon_2$, whose high column density significantly affects the observed $T_{\rm rot}$, as explained later in this Section (see also Table C1). Conversely, the behaviour of the HCNH$^+$ curve is influenced by the much lower dipole moment (about 10 times below the other molecules, also reported in Table C1), leading to a lower **effective** critical density (as shown in the right panel of Fig. C1), thus to a more efficient excitation of higher J levels, and consequently to a broadening of the Q branch.

As discussed above, the width of the Q-branch absorption traces $T_{\rm rot}$ of the ground state. For increasing $n_{\rm H_2}$, $T_{\rm rot}$ increases, tending to $T_{\rm kin}$, and making broader the observed Q-branch absorption. Therefore, we define the effective critical density, $n^{\rm eff}_{\rm crit}$, for each band as the value of $n_{\rm H_2}$ at which the observed full width at half-maximum (FWHM) of the Q-branch reaches 99 per cent of the FWHM of the

band under LTE conditions (i.e. $T_{\rm rot} = T_{\rm kin}$). We note that we cannot adopt the critical densities of the individual rotational transitions (e.g. Shirley 2015) since the Q-branch is sensitive to the population of all the ground state rotational levels. We computed NLTE models with $T_{\rm kin}$ from 50 to 200 K and $n_{\rm H_2}$ ranging from 10^4 to 10^9 cm^{-3}, with the same column densities reported in Table 1. The right panel of Fig. C1 shows $n_{\rm crit}^{\rm eff}$ of each band as a function of $T_{\rm kin}$. The $HCNH^+$ curve stands apart from the others, with $n_{\rm crit}^{\rm eff}$ more than one dex lower than those of the other bands. This indicates that collisions with H_2 play a significant role in allowing $HCNH^+$ to reach equilibrium more efficiently with radiation since $T_{\rm rot}$ starts at higher values than for the other molecules (see the left panel of Fig. C1).

The opacity of the band can also significantly affect the observed $T_{\rm rot}$. This is illustrated by the two HCN curves in Fig. C1, which correspond to the range of HCN column density values from $N = 2.0\times10^{18}$ cm^{-2} (upper curve) to $N = 6.6\times10^{17}$ cm^{-2} (lower curve; see Table 1). Thus, higher column densities, hence higher opacities, can increase the observed $T_{\rm rot}$ of the bands.

Consequently, if IR pumping, NLTE excitation, and opacity effects are taken into account, it is plausible that all these molecular bands originate at the same physical region close to the core of IRAS 07251, even if they exhibit different observed $T_{\rm rot}$ (Table 1).

3.2 Comparison with chemical models

To shed light on the origin of the observed molecules, we carried out chemical modelling calculations using a model for obscured dense molecular clouds (Agúndez & Wakelam 2013). We adopted a gas $T_{\rm kin}$ of 200 K (according to the gas temperature reported by García-Bernete et al. submitted), a high visual extinction of 30 mag to prevent UV photons from playing a role, roughly solar elemental abundances including dust depletion (table 3 of Agúndez & Wakelam 2013; see also Appendix D for a discussion on this assumption), and the gas-phase chemical network corresponding to the latest release of the UMIST Database for Astrochemistry (Millar et al. 2024). We varied the cosmic-ray ionization rate of H_2 to cover the range $\zeta_{\rm H_2}/n_{\rm H} = 10^{-21}$–$10^{-15}$ cm^3 s^{-1}. We note that, testing the results through variations in $n_{\rm H}$, steady state abundances, in which we focus here, are only sensitive to the $\zeta_{\rm H_2}/n_{\rm H}$ ratio, but not to these two parameters separately (see e.g. Padovani, Galli & Glassgold 2009; Ceccarelli et al. 2014). In Fig. 2, we compare the calculated abundances relative to H nuclei with the observed values as a function of the $\zeta_{\rm H_2}/n_{\rm H}$ ratio. We observe that the H_3^+ prediction matches the corresponding observed value at a $\log(\zeta_{\rm H_2}/n_{\rm H}\,[{\rm cm^3\,s^{-1}}])$ of ~ -18.2.

The left panel of Fig. 2 shows H_3^+ together with HCN, HNC, and $HCNH^+$, which are closely related through the protonation reactions $H_3^+ + {\rm HCN(HNC)} \rightarrow HCNH^+ + H_2$, the dissociative recombination reaction $HCNH^+ + e^- \rightarrow {\rm HCN(HNC)} + H$, as well as the neutral reaction HNC + H → HCN + H. The ion route involving $HCNH^+$ is expected to produce HCN and HNC with similar yields. However, the neutral–neutral reaction can isomerize HNC into HCN at high temperatures (Schilke et al. 1992), as its rate coefficient $k(T) = 10^{-10}e^{E_a/T}$ depends on the activation energy barrier (E_a), which in our models is set at 1200 K, following chemical models of ISM clouds (Graninger et al. 2014). We observe that models underestimate the absolute abundances of these species by a factor of ∼10–100. However, the relative abundance $HCNH^+$/(HCN + HNC) ratio is consistent between models and observations within a factor of <4 (0.019 versus 0.005–0.014) since this ratio is driven by the protonation reactions and mostly depends on the $\zeta_{\rm H_2}/n_{\rm H}$ ratio and their relative abundances. However, the predicted HCN/HNC abundance ratio is lower than the observed ratio (2.3 versus 12–37). This suggests that the neutral reaction has not begun depleting HNC and might indicate that the barrier of this reaction is lower than the assumed value (e.g. Hirota et al. 1998) or that the H abundance is higher than that predicted by the models, which depends on the relatively uncertain assumed H_2 formation rate (3×10^{-17} cm^3 s^{-1}; Wakelam et al. 2017).

In the right panel of Fig. 2, we present the fractional abundances predicted for all the detected cations (Table. 1). As expected from previous studies (e.g. Agúndez et al. 2018; Gaches, Offner & Bisbas 2019), HCO^+ is the most abundant cation, after H_3^+, in both models and observations. There is a good agreement, within a factor of 4, for HCO^+ and N_2H^+. However, $HCNH^+$ is underestimated by the models. This discrepancy likely arises from the underestimation of HCN and HNC (as discussed above), which leads to lower predicted abundances of $HCNH^+$. Observations of HCO^+ and N_2H^+ intersect the models at $\log(\zeta_{\rm H_2}/n_{\rm H}\,[{\rm cm^3\,s^{-1}}]) \sim -19.1$, differently from the H_3^+ intersection at $\log(\zeta_{\rm H_2}/n_{\rm H}\,[{\rm cm^3\,s^{-1}}]) \sim -18.2$.[1] This discrepancy may arise because the model adopts a single constant density for all molecules, suggesting that H_3^+ may have a slightly lower density compared to HCO^+ and N_2H^+. This is consistent with predictions from theoretical models (e.g. Padovani & Galli 2011; Padovani et al. 2013) and observational evidence (e.g. Sabatini, Bovino & Redaelli 2023; Socci et al. 2024), which suggest that ionization from cosmic rays depends on local physical conditions and may be attenuated when penetrating denser gas regions. In conclusion, our results support a scenario in which the observed molecules originate from a CRDR, with H_3^+ playing a key role in shaping the chemistry of the ISM (see also models from Harada, Herbst & Wakelam 2010 and Bayet et al. 2011).

4 SUMMARY AND CONCLUSIONS

We analysed absorption features from the fundamental ro-vibrational bands of HCO^+ ν_2, $HCNH^+$ ν_4 and ν_5, N_2H^+ ν_2, HC_3N ν_5, and HNC ν_2 detected by *JWST*/MIRI MRS in the eastern nucleus of the ULIRG IRAS 07251−0248 ($d \sim 400$ Mpc). Based on the physical properties inferred from these bands and the comparison with chemical models, we draw the following conclusions:

(i) *Outflowing warm molecular gas.* We find that the molecular absorptions are blueshifted by 160 km s^{-1} relative to the rest-frame velocity of this object. From the LTE models, we find high rotational temperatures: $HCNH^+$ ν_4 and ν_5 and HCN $2\nu_2$ exhibit the highest $T_{\rm rot}$ from ∼150 to ∼185 K, while 40–120 K, are measured for the remaining species. This suggests that the absorptions are produced in a expanding warm molecular shell. Using equation 11 of González-Alfonso et al. (2017) and assuming a shell radius of 20–75 pc, the observed $N_{\rm H}$ and velocity correspond to a mass outflow rate of $\dot{M}$ ∼ 90–330 $M_\odot$ yr^{-1}, and could be the inner launching region of the larger scale (170 pc) and faster (380 km s^{-1}) cold molecular outflow ($\dot{M} \sim 50\,M_\odot$ yr^{-1}) reported by Lamperti et al. (2022).

(ii) *Evidence for IR radiative pumping*. The observed $T_{\rm rot}$ values vary by up to 140 K. These differences can be explained by a radiative transfer model under NLTE condition. In this context,

[1] There is another solution at $\log \zeta_{\rm H_2}/n_{\rm H} \sim -17.5$, however this solution lies close to a discontinuity in the molecular abundances, which is related to the bistability of dark cloud chemistry (Le Bourlot et al. 1993). Near this discontinuity, a slight increase of $\zeta_{\rm H2}/n_{\rm H}$ results in a sharp decrease in the molecular abundances. Thus, although this solution is physically possible, we favour the lower $\zeta_{\rm H_2}/n_{\rm H}$ solution, which lies in a more stable regime of the chemical models.

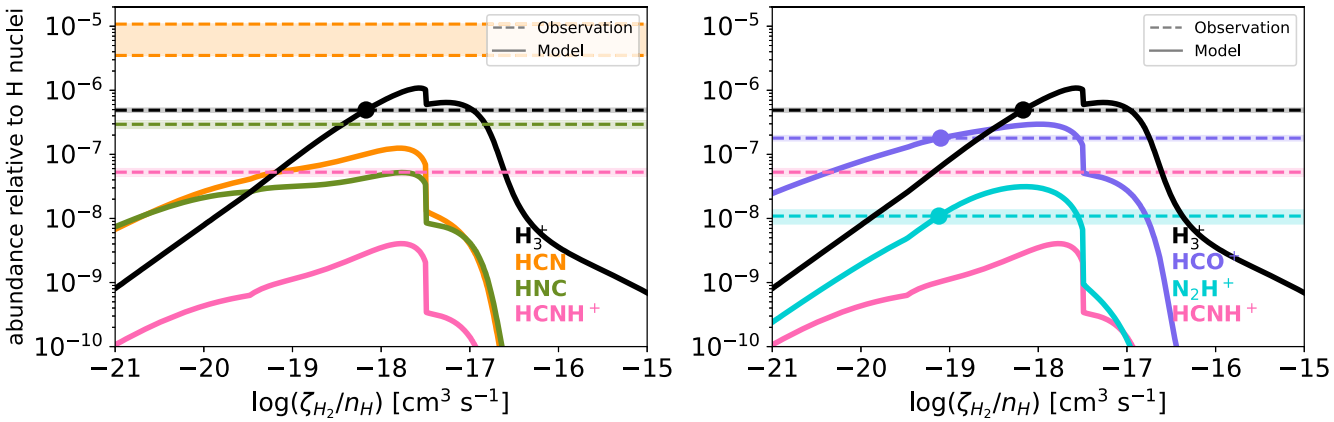

Figure 2. Predicted fractional abundances by chemical models as function of the ζ_{H_2}/n_{H_2} ratio (solid curves) and observed values (horizontal dashed lines) with shaded area for the corresponding uncertainties. We assumed a H column density of $N_H = 1.89 \times 10^{23}$cm^{-2} according to Pereira-Santaella et al. (2024b). H_3^+ (black), HCN (orange), HNC (green), $HCNH^+$ (pink) are presented in the left panel. Both observed abundances from García-Bernete et al. submitted are shown for HCN, with the uncertainty represented by their difference. The median value is shown for the observed $HCNH^+$ abundances reported in Table 1. The cations H_3^+ (black), HCO^+ (purple), N_2H^+ (turquoise), and $HCNH^+$ (pink) are shown in the right panel. The black point indicates where the H_3^+ model coincides with the observed abundance from Pereira-Santaella et al. (2024b), while the purple and turquoise points correspond to the intersections between observations and models of HCO^+ and N_2H^+, respectively.

infrared radiative pumping is a viable excitation mechanism. This supports the idea that all molecules originate from the same shell near the core of IRAS 07251.

(iii) *CRDR chemistry in IRAS 07251*. We find that CR play a key role in the chemistry of the nuclear ISM in IRAS 07251. According to chemical models, the fractional abundances of the observed molecular cations (H_3^+, HCO^+, $HCNH^+$, and N_2H^+) are consistent with a CRDR with a high $\log(\zeta_{H_2}/n_H\,[\mathrm{cm^3\,s^{-1}}])$ in the range of -19.1 to -18.2. The lower value is derived from HCO^+ and N_2H^+, which are believed to trace denser gas than H_3^+. This result is consistent with theoretical predictions suggesting a decrease in CRIR in denser environments.

This study demonstrates the capability of *JWST* to probe the ISM chemistry through several molecular ro-vibrational bands, transitions that were previously unexplored in extragalactic sources due to limitations in sensitivity and resolution. These bands are also crucial for probing the excitation mechanisms dominating the region near the galaxy's core.

ACKNOWLEDGEMENTS

The authors acknowledge the GOALS team for developing their observing programmes. GS and MPS acknowledge support under grant CNS2023-145506 funded by MCIN/AEI/10.13039/501100011033 and the European Union NextGenerationEU/PRTR. MPS acknowledges support under grant RYC2021-033094-I funded by MCIN/AEI/10.13039/501100011033 the European Union NextGenerationEU/PRTR. MPS, EGA, JRG, and MGSM thank the Spanish MCINN for funding support under grant PID2023-146667NB-I00 funded by MCIN/AEI/10.13039/501100011033. MA acknowledges support under grant PID2023-147545NB-I00. IGB was supported by the Programa Atracción de Talento Investigador 'César Nombela' via grant 2023-T1/TEC-29030 funded by the Community of Madrid. EG-A thanks the Spanish MICINN for support under project PID2022-137779OB-C41. This work is based on observations made with the NASA/ESA/CSA James Webb Space Telescope. The data were obtained from the Mikulski Archive for Space Telescopes at the Space Telescope Science Institute, which is operated by the Association of Universities for Research in Astronomy, Inc., under NASA contract NAS 5–03127 for *JWST*; and from the European JWST archive (eJWST) operated by the ESAC Science Data Centre (ESDC) of the European Space Agency. These observations are associated with programme #3368.

DATA AVAILABILITY

The data are available in the *JWST* Science Archive at https://jwst.esac.esa.int/archive/, under proposal ID #3368.

REFERENCES

Agúndez M., Wakelam V., 2013, Chem. Rev., 113, 8710
Agúndez M., Roueff E., Le Petit F., Le Bourlot J., 2018, A&A, 616, A19
Agúndez M., Marcelino N., Cernicharo J., Roueff E., Tafalla M., 2019, A&A, 625, A147
Altman R. S., Crofton M. W., Oka T., 1984, J. Chem. Phys., 81, 4255
Amano T., 1983, J. Chem. Phys., 79, 3595
Amano T., Hirao T., Takano J., 2005, J. Mol. Spectrosc., 234, 170
Amano T., Hashimoto K., Hirao T., 2006, J. Mol. Struct., 795, 190
Argyriou I. et al., 2023, A&A, 675, A111
Baba S., Nakagawa T., Isobe N., Shirahata M., 2018, ApJ, 852, 83
Balança C., Scribano Y., Loreau J., Lique F., Feautrier N., 2020, MNRAS, 495, 2524
Barber R. J., Strange J. K., Hill C., Polyansky O. L., Mellau G. C., Yurchenko S. N., Tennyson J., 2014, MNRAS, 437, 1828
Bayet E., Williams D. A., Hartquist T. W., Viti S., 2011, MNRAS, 414, 1583
Blackman G. L., Brown R. D., Godfrey P. D., Gunn H. I., 1976, Nature, 261, 395
Bop C. T., Lique F., 2023, J. Chem. Phys., 158, 074304
Botschwina P., 1986, Chem. Phys. Lett., 124, 382
Bovino S., Ferrada-Chamorro S., Lupi A., Schleicher D. R. G., Caselli P., 2020, MNRAS, 495, L7
Bruderer S., Doty S. D., Benz A. O., 2009, ApJS, 183, 179
Buiten V. A. et al., 2024, ApJ, 966, 166
Buiten V. et al., 2025, preprint (arXiv:2502.10271)
Bushouse H. et al., 2023, JWST Calibration Pipeline, Zenodo, Version 1.12.4
Cazzoli G., Cludi L., Buffa G., Puzzarini C., 2012, ApJS, 203, 11

Ceccarelli C., Dominik C., López-Sepulcre A., Kama M., Padovani M., Caux E., Caselli P., 2014, ApJ, 790, L1
Davies P. B., Rothwell W. J., 1984, J. Chem. Phys., 81, 5239
Davies P. B., Rothwell W. J., Hamilton P. A., 1984, J. Chem. Phys., 81, 1598
Denis-Alpizar O., Stoecklin T., Dutrey A., Guilloteau S., 2020, MNRAS, 497, 4276
Donnan F. R., García-Bernete I., Rigopoulou D., Pereira-Santaella M., Alonso-Herrero A., Roche P. F., Hernán-Caballero A., Spoon H. W. W., 2023, MNRAS, 519, 3691
Donnan F. R., García-Bernete I., Rigopoulou D., Pereira-Santaella M., Roche P. F., Alonso-Herrero A., 2024, MNRAS, 529, 1386
Dumouchel F., Faure A., Lique F., 2010, MNRAS, 406, 2488
Ebenstein W. L., Muenter J. S., 1984, J. Chem. Phys., 80, 3989
Endres C. P., Schlemmer S., Schilke P., Stutzki J., Müller H. S. P., 2016, J. Mol. Spectrosc., 327, 95
Esposito F., Vallini L., Pozzi F., Casasola V., Mingozzi M., Vignali C., Gruppioni C., Salvestrini F., 2022, MNRAS, 512, 686
Falstad N. et al., 2021, A&A, 649, A105
Faure A., Lique F., Wiesenfeld L., 2016, MNRAS, 460, 2103
Fontani F. et al., 2017, A&A, 605, A57
Foster S. C., McKellar A. R. W., 1984, J. Chem. Phys., 81, 3424
Foster S. C., McKellar A. R. W., Sears T. J., 1984, J. Chem. Phys., 81, 578
Fuente A. et al., 2019, A&A, 624, A105
Gaches B. A. L., Offner S. S. R., 2018, ApJ, 861, 87
Gaches B. A. L., Offner S. S. R., Bisbas T. G., 2019, ApJ, 878, 105
García-Bernete I., Rigopoulou D., Aalto S., Spoon H. W. W., Hernán-Caballero A., Efstathiou A., Roche P. F., König S., 2022a, A&A, 663, A46
García-Bernete I. et al., 2022b, A&A, 666, L5
García-Bernete I. et al., 2024a, A&A, 681, L7
García-Bernete I., Pereira-Santaella M., González-Alfonso E., Rigopoulou D., Efstathiou A., Donnan F. R., Thatte N., 2024b, A&A, 682, L5
Glasse A. et al., 2015, PASP, 127, 686
González-Alfonso E. et al., 2013, A&A, 550, A25
González-Alfonso E. et al., 2015, ApJ, 800, 69
González-Alfonso E. et al., 2017, ApJ, 836, 11
González-Alfonso E., García-Bernete I., Pereira-Santaella M., Neufeld D. A., Fischer J., Donnan F. R., 2024, A&A, 682, A182
Gordon I. E. et al., 2022, J. Quant. Spec. Radiat. Transf., 277, 107949
Graninger D. M., Herbst E., Öberg K. I., Vasyunin A. I., 2014, ApJ, 787, 74
Hansson A., Watson J. K. G., 2005, J. Mol. Spectrosc., 233, 169
Harada N., Herbst E., Wakelam V., 2010, ApJ, 721, 1570
Harada N. et al., 2024, ApJS, 271, 38
Havenith M., Zwart E., Leo Meerts W., Ter Meulen J. J., 1990, J. Chem. Phys., 93, 8446
Heninger M., Lauvergnat D., Lemaire J., Boissel P., Mauclaire G., Marx R., 2003, Int. J. Mass Spectrom., 223, 669
Hernández Vera M., Lique F., Dumouchel F., Hily-Blant P., Faure A., 2017, MNRAS, 468, 1084
Hirao T., Yu S., Amano T., 2008, J. Mol. Spectrosc., 248, 26
Hirota E., Endo Y., 1988, J. Mol. Spectrosc., 127, 527
Hirota T., Yamamoto S., Mikami H., Ohishi M., 1998, ApJ, 503, 717
Ho W.-C., Blom C. E., Liu D.-J., Oka T., 1987, J. Mol. Spectrosc., 123, 251
Holden L. R., Tadhunter C., Audibert A., Oosterloo T., Ramos Almeida C., Morganti R., Pereira-Santaella M., Lamperti I., 2024, MNRAS, 530, 446
Hung C.-L. et al., 2014, ApJ, 791, 63
Imanishi M., Nakanishi K., Izumi T., 2016, ApJ, 825, 44
Imanishi M., Baba S., Nakanishi K., Izumi T., 2023, ApJ, 950, 75
Jiménez-Donaire M. J. et al., 2023, A&A, 676, L11
Johnson, R. D., IIIed., 2022, NIST Computational Chemistry Comparison and Benchmark Database. NIST Standard Reference Database Number 101, NIST, Gaithersburg
Kabbadj Y., Huet T. R., Rehfuss B. D., Gabrys C. M., Oka T., 1994, J. Mol. Spectrosc., 163, 180
Kajita M., Kawaguchi K., Hirota E., 1988, J. Mol. Spectrosc., 127, 275
Kálosi Á., Dohnal P., Shapko D., Roučka Š., Plašil R., Johnsen R., Glosík J., 2017, J. Instrum., 12, C10010
Kawaguchi K., Yamada C., Saito S., Hirota E., 1985, J. Chem. Phys., 82, 1750
Keim E. R., Polak M. L., Owrutsky J. C., Coe J. V., Saykally R. J., 1990, J. Chem. Phys., 93, 3111
Labiano A. et al., 2021, A&A, 656, A57
Lahuis F. et al., 2007, ApJ, 659, 296
Lamperti I. et al., 2022, A&A, 668, A45
Lattanzi V., Walters A., Drouin B. J., Pearson J. C., 2007, ApJ, 662, 771
Le Bourlot J., Pineau des Forets G., Roueff E., Schilke P., 1993, ApJ, 416, L87
Liu D.-J., Lee S.-T., Oka T., 1988, J. Mol. Spectrosc., 128, 236
Martin J. M. L., Taylor P. R., Lee T. J., 1993, J. Chem. Phys., 99, 286
Meier D. S., Turner J. L., 2012, ApJ, 755, 104
Millar T. J., Walsh C., Van de Sande M., Markwick A. J., 2024, A&A, 682, A109
Nakanaga T., Ito F., Sugawara K., Takeo H., Matsumura C., 1990, Chem. Phys. Lett., 169, 269
Neese C. F., Kreynin P. S., Oka T., 2013, J. Phys. Chem. A, 117, 9899
Neufeld D. A., Wolfire M. G., 2017, ApJ, 845, 163
Nomoto K., Hashimoto M., Tsujimoto T., Thielemann F. K., Kishimoto N., Kubo Y., Nakasato N., 1997, Nucl. Phys. A, 616, 79
Oka T., 2013, Chem. Rev., 113, 8738
Onishi S. et al., 2021, ApJ, 921, 141
Padovani M., Galli D., 2011, A&A, 530, A109
Padovani M., Galli D., Glassgold A. E., 2009, A&A, 501, 619
Padovani M., Hennebelle P., Galli D., 2013, A&A, 560, A114
Papadopoulos P. P., 2010, ApJ, 720, 226
Pereira-Santaella M. et al., 2021, A&A, 651, A42
Pereira-Santaella M. et al., 2022, A&A, 665, L11
Pereira-Santaella M., González-Alfonso E., García-Bernete I., García-Burillo S., Rigopoulou D., 2024a, A&A, 681, A117
Pereira-Santaella M. et al., 2024b, A&A, 689, L12
Pety J. et al., 2017, A&A, 599, A98
Pineda J. E. et al., 2024, A&A, 686, A162
Podio L., Lefloch B., Ceccarelli C., Codella C., Bachiller R., 2014, A&A, 565, A64
Redaelli E., Bovino S., Lupi A., Grassi T., Gaete-Espinoza D., Sabatini G., Caselli P., 2024, A&A, 685, A67
Sabatini G., Bovino S., Redaelli E., 2023, ApJ, 947, L18
Santa-Maria M. G., Goicoechea J. R., Etxaluze M., Cernicharo J., Cuadrado S., 2021, A&A, 649, A32
Sasada H., Amano T., 1990, J. Chem. Phys., 92, 2248
Schilke P., Walmsley C. M., Pineau Des Forets G., Roueff E., Flower D. R., Guilloteau S., 1992, A&A, 256, 595
Sears T. J., 1985, J. Opt. Soc. Am. B, 2, 786
Shirley Y. L., 2015, PASP, 127, 299
Siller B. M., Hodges J. N., Perry A. J., McCall B. J., 2013, J. Phys. Chem. A, 117, 10034
Silva W. G. D. P., Bonah L., Schmid P. C., Schlemmer S., Asvany O., 2024, J. Chem. Phys., 160, 071101
Socci A., Sabatini G., Padovani M., Bovino S., Hacar A., 2024, A&A, 687, A70
Spoon H. W. W. et al., 2004, ApJS, 154, 184
Tanaka K., Kawaguchi K., Hirota E., 1986, J. Mol. Spectrosc., 117, 408
Verhoeve P., Zwart E., Versluis M., Drabbels M., ter Meulen J. J., Meerts W. L., Dymanus A., McLay D. B., 1990, Rev. Sci. Instrum., 61, 1612
Wakelam V. et al., 2017, Mol. Astrophys., 9, 1
Wells M. et al., 2015, PASP, 127, 646
Western C. M., 2017, J. Quant. Spec. Radiat. Transf., 186, 221
Yamaguchi Y., Richards C. A., Jr, Schaefer H. F., III, 1994, J. Chem. Phys., 101, 8945
Yu S., Pearson J. C., Drouin B. J., Crawford T., Daly A. M., Elliott B., Amano T., 2015, J. Mol. Spectrosc., 314, 19

APPENDIX A: MIRI/MRS DATA REDUCTION

IRAS 07251−0248 was observed with *JWST* as part of the Cycle 2 Large Programme #3368 (P.I. L. Armus and A. Evans). In this Letter, we analyse the integral-field spectroscopy obtained with MIRI/MRS

in the 4.9–28.1 μm range with a spectral resolution of $R \sim$1300–3700 (Labiano et al. 2021).

The raw data were processed using the *JWST* calibration pipeline (version 1.12.4; Bushouse et al. 2023) and context 1253. In addition to the standard data reduction steps, we performed a number of custom steps to reduce the effect of cosmic rays and hot and cold pixels. We extracted the spectrum of the E nucleus of IRAS 07251−0248 assuming that it is dominated by a point source at the angular resolution of MRS (0.″25–0.″60 depending on the wavelength). Further details on the data reduction and extraction of the nuclear spectrum can be found in Pereira-Santaella et al. (2022) and García-Bernete et al. (2022b, 2024a).

APPENDIX B: MOLECULAR PARAMETERS

We analysed the mid-IR ro-vibrational absorption bands of five molecules (HCO^+, $HCNH^+$, N_2H^+, HC_3N, and HNC). In this appendix, we describe the spectroscopic parameters as well as the collisional rate coefficients used in this Letter.

For HNC, we used the line list provided by Barber et al. (2014), part of the ExoMol data base, and the collisional coefficients from Dumouchel, Faure & Lique (2010) and Hernández Vera et al. (2017). The HITRAN data base (Gordon et al. 2022) was used for the HC_3N line list together with the collisional coefficients calculated by Faure, Lique & Wiesenfeld (2016).

For the remaining three molecular cations (HCO^+, $HCNH^+$, and N_2H^+), we used the wavelengths of rotational and ro-vibrational transitions from laboratory measurements to determine the best-fitting molecular spectroscopic constants of all the fundamental vibrational states. We performed this fit using PGOPHER (Western 2017). All these cations are linear molecules with a $^1\Sigma$ ground electronic state. Therefore, within PGOPHER, we used a Hamiltonian with a rotational operator, including up to the sextic (H) and quartic (D) centrifugal distortion constants for the ground and vibrationally excited states, respectively, and, for the bending modes, we also included the l-type interaction with the l-type doubling constant q and its high order correction, q_D, as free parameters. The origin of the band is also determined during the fit.

We used the strength of the vibrational bands, calculated theoretically or measured in the laboratory when available, to determine the Einstein A coefficient of the band, A_{band}. Then, the Einstein A coefficient of each ro-vibrational transition, A_{ul} was computed using the relation $A_{ul} = A_{band}(\nu_{ul}/\nu_0)^3 S_{J_l}^{\Delta J}/(2J_u+1)$, where ν_{ul} and ν_0 are the frequency of the ro-vibrational transition between levels u and l and the origin of the vibrational band, respectively, J_u is the quantum number J of the upper level u, and $S_{J_l}^{\Delta J}$ is the Hönl–London factor (e.g. Hansson & Watson 2005). The line lists and spectroscopic constants are available from the authors upon request and will be presented in a future work (Pereira-Santaella in preparation).

We note that the fundamental υ_2 bands of HCO^+ and N_2H^+ are included in the CDMS data base (Endres et al. 2016). For these two vibrational bands, we obtain wavelengths and Einstein A coefficients in good agreement with those in CDMS with differences <0.5 km s^{-1} for the position of the lines and <2 per cent for the A coefficients.

B1 HCO^+

For the fit of the spectroscopic constants, we used the rotational transitions presented in Hirota & Endo (1988), Lattanzi et al. (2007), Hirao, Yu & Amano (2008), and Cazzoli et al. (2012), the υ_2 fundamental band measured by Davies & Rothwell (1984) and Kawaguchi et al. (1985), and the υ_1 and υ_3 stretching modes from Amano (1983), Davies, Rothwell & Hamilton (1984), Foster, McKellar & Sears (1984), Neese, Kreynin & Oka (2013), and Siller et al. (2013). The strength of the bands are taken from the experiments by Keim et al. (1990) and the calculations by Martin, Taylor & Lee (1993). The collisional rate coefficients with H_2 are from Denis-Alpizar et al. (2020).

B2 N_2H^+

To obtain the spectroscopic constants, we fitted rotational transitions (Verhoeve et al. 1990; Amano, Hirao & Takano 2005; Cazzoli et al. 2012; Yu et al. 2015), fundamental υ_2 ro-vibrational transitions (Sears 1985), and υ_1 and υ_3 transition from Foster & McKellar (1984), Nakanaga et al. (1990), Sasada & Amano (1990), Kabbadj et al. (1994), and Kálosi et al. (2017). The strength of the bands are from the experiments by Keim et al. (1990) and the calculations by Heninger et al. (2003). We used the collisional rate coefficients with H_2 from Balança et al. (2020).

B3 $HCNH^+$

We fitted the rotational transitions (Amano, Hashimoto & Hirao 2006; Silva et al. 2024), and the ro-vibrational transitions from the three stretching modes (υ_1, υ_2, and υ_3; Altman, Crofton & Oka 1984; Kajita, Kawaguchi & Hirota 1988; Liu, Lee & Oka 1988) and from the two bending modes (υ_4 and υ_5; Tanaka, Kawaguchi & Hirota 1986; Ho et al. 1987) to obtain the spectroscopic constants. For the strength of the vibrational bands, we calculated the average value from the different levels of quantum theory calculations in the CCCBDB data base (Johnson 2022). The collisional rate coefficients with H_2 are from Bop & Lique (2023).

APPENDIX C: NLTE MODELS

In this Section, we show Fig. C1, which is invoked to illustrate how the infrared radiative pumping mechanism can explain the range of T_{rot} values measured from the observed spectra. This figure is discussed in Section 3.1, and in Table C1 we report the relevant quantities mentioned in the discussion, namely: the Einstein A_{ul} coefficients, the Einstein B_{ul} coefficients normalized to that of

Table C1. Einstein coefficients, dipole moments, and effective critical densities of the ro-vibrational transitions shown in Fig. C1.

Name(1)	A_{ul} (2) (s^{-1})	$B_{lu}/B_{lu}^{HCO^+}$ (3)	Dipole moment(4) (D)	n_{crit}^{eff} (5) (cm^{-3})	Ref.(6)
HCO^+ υ_2	1.46	1	3.89	4.33×10^8	(Y94)
N_2H^+ υ_2	8.13	9.8	3.4	3.80×10^8	(H90)
$HCNH^+$ υ_5	9.14	13.3	0.29	9.71×10^5	(B86)
HNC υ_2	3.37	13.2	3.05	7.03×10^7	(B76)
HCN $2\upsilon_2$	2.09	0.3	2.98	7.03×10^7	(E84)
HCN υ_2	1.83	2.0	2.98	7.03×10^7	(E84)

Note. (1) Vibrational band; (2) Einstein A_{ul} coefficient corresponding to the Q(1) transition, except for HCN $2\upsilon_2$ in which case it corresponds to the R(1) transition; (3) Einstein B_{lu} coefficient normalized to the HCO^+ υ_2 B_{lu} coefficient; (4) Dipole moment; (5) n_{crit}^{eff} at 200 K; (6) References for the dipole moment: (Y94) Yamaguchi, Richards & Schaefer (1994), (H90) Havenith et al. (1990), (B86) Botschwina (1986), (B76) Blackman et al. (1976), (E84) Ebenstein & Muenter (1984).

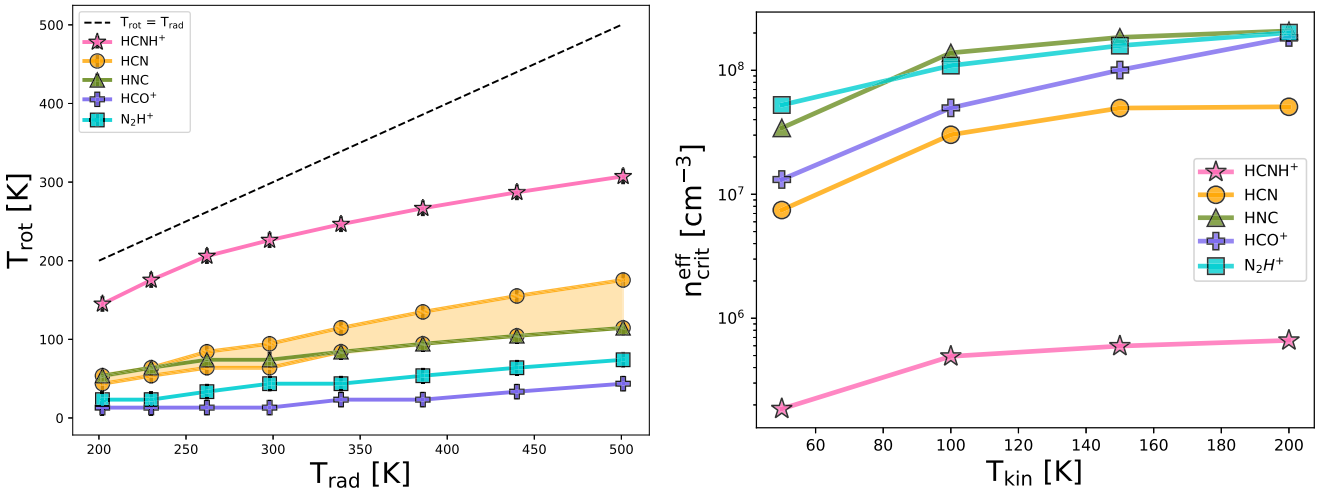

Figure C1. Expected rotational temperature of non-LTE models and effective critical densities for the bands analysed in the work. In both panels the same ro-vibrational bands are shown: $HCNH^+$ (ν_5; pink stars), HCN (orange circles), HNC (green triangles), HCO^+ (purple pluses), N_2H^+ (turquoise squares). Left panel: T_{rot} from simulated NLTE absorption bands as a function of the radiation temperature (T_{rad}). The black dashed line indicate when T_{rot} is equal to T_{rad}. The two HCN curves correspond to the two columns for bands $2\nu_2$ (upper curve) and ν_2 (bottom curve) reported in Table 1. Right panel: effective critical density of the ro-vibrational band versus T_{kin}.

HCO^+, the dipole moments, and n^{eff}_{crit} at 200 K for each molecule presented in Fig. C1.

APPENDIX D: INITIAL ABUNDANCES OF THE CHEMICAL MODEL

We explored how predictions of molecular fractional abundances change when varying the initial elemental abundances in the chemical model. Roughly solar elemental abundances, with a C/O ratio of ∼0.54, are adopted in the models presented in Section 3.2. In Fig. D1, we compare these models (solid curves) with predictions using initial top-heavy elemental abundances (dash-dotted curves). The top-heavy abundances are obtained by increasing the oxygen abundance by a factor of four and the remaining elements by a factor two, resulting in a C/O ratio of ∼0.27, typical of a top-heavy initial mass function (e.g. Nomoto et al. 1997). Such initial conditions may be suitable in the case of recent star formation activity. The final predictions experience some changes if a top-heavy scenario is assumed. Essentially, CO increases its abundance while those molecules containing carbon (but not oxygen) decrease their abundance as a consequence of the lower C/O ratio. This affects to HCN and HNC. A further consequence is a general decrease in the abundance of cations such as N_2H^+ and $HCNH^+$, which is in part caused by an enhanced destruction of H_3^+ with CO. Although the abundances of HCN, HNC, and $HCNH^+$ decrease due to the lower availability of carbon in the top-heavy regime, the abundance ratio $HCNH^+/(HCN + HNC)$ remains relatively unchanged. It is also worth noting that the discontinuity due to bistability almost vanishes and the abundance peaks shift to higher ζ_{H_2}/n_H ratios.

APPENDIX E: CHEMICAL MODEL COMPARED TO ANALYTICAL PREDICTIONS

Pereira-Santaella et al. (2024b) predicted the H_3^+ fractional abundance as function of ζ_{H_2}/n_H using equation 2 of Neufeld & Wolfire (2017), which was derived for diffuse and translucent clouds. Following González-Alfonso et al. (2013), they adopted a constant electron fractional abundance in the range $x_e = (1.5–5) \times 10^{-4}$ (derived from models by Bruderer, Doty & Benz 2009 for relative high values of ζ_{H_2}/n_H) and a molecular fraction (f_{H_2}) given by the maximum value of equation 2 of González-Alfonso et al. (2013). There are two main differences compared to the chemical model used in this work: (1) the analytical formulation assumes a constant electron abundance, and (2) metals are not included in the calculations (only x_e and f_{H_2} are considered). In Fig. E1, we compare these predictions. Our molecular fraction (solid pink line) starts decreasing at lower $\log(\zeta_{H_2}/n_H)$ than their f_{H_2} (dashed pink line). This is due to the lower R_f assumed in this work (3×10^{-17} versus 5×10^{-17} cm^3 s^{-1}) and due to the significant destruction of H_2 by OH^+ and O^+ in the $\log(\zeta_{H_2}/n_H$ [cm^3 s^{-1}]) ∼ −17−−15 range. This difference is responsible for the shift of the H_3^+ abundance peak to lower ζ_{H_2}/n_H of $10^{-17.6}$ cm^3 s^{-1} versus the peak at $\zeta_{H_2}/n_H = 10^{-15.9}$ cm^3 s^{-1} predicted by the analytical model.

If metals are excluded from our chemical network, the predicted molecular fractions match the analytical results obtained under consistent assumptions (i.e. using $R_f = 3\times10^{-17}$ cm^3 s^{-1} instead of the 5×10^{-17} cm^3 s^{-1}; see dash-dotted and dotted pink curves). However, under these conditions, our model matches the analytical H_3^+ abundance only in the range $-17.8 \leq \log(\zeta_{H_2}/n_H)$ [cm^3 s−1] ≤ -17.3, where the electron abundances from the chemical model overlap with the range assumed by Pereira-Santaella et al. 2024b. Outside this interval, the electron abundance in our chemical model is greater at $\log(\zeta_{H_2}/n_H)$ [cm^3 s−1] ≥ -17.3 (lower at $\log(\zeta_{H_2}/n_H)$ [cm^3 s−1] ≤ -17.8) than the constant range, thereby enhancing (reducing) H_3^+ destruction. This results in lower (higher) H_3^+ abundances (see the dash-dotted black line) compared to the predictions based on a constant x_e.

In the right panel of Fig. E1, we present a power-law fit to the x_e predictions given by the chemical model. For the model in which metals are not included we obtain

$$\log(x_e) = 0.67 \log(\zeta_{H_2}/n_H) + 8.14, \quad \text{(E1)}$$

which corresponds to the green dash-dotted line. In the case in which metals are included, we performed a piecewise power-law fit of x_e in

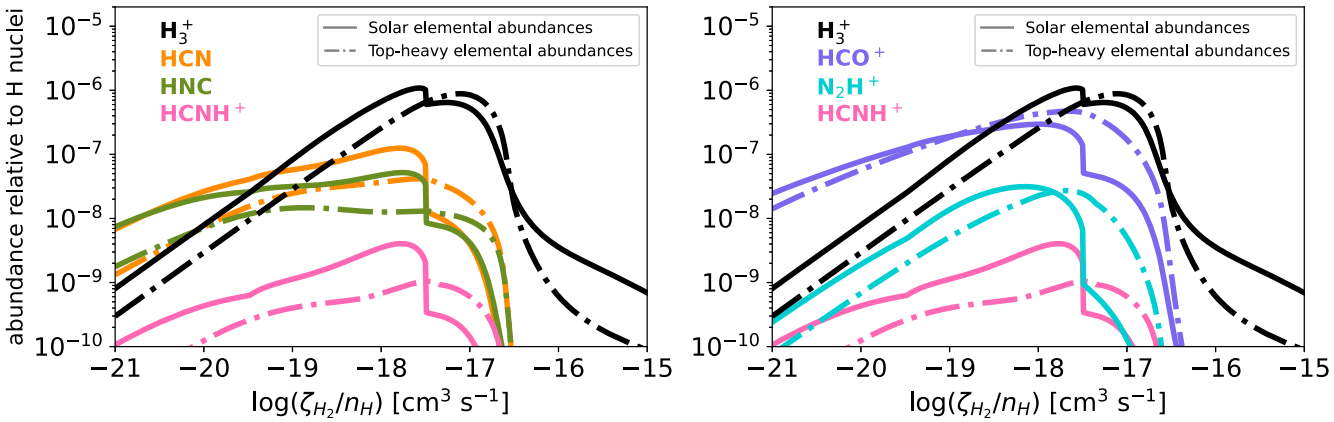

Figure D1. Predictions of molecular fractional abundances as a function of the ζ_{H_2}/n_H ratio. The solid curves are the same shown in Fig. 2, which are obtained using initial solar elemental abundances. The dash-dotted curves represent predictions for a cloud with top-heavy elemental abundances. The same colours as Fig. 2 are used to distinguish the different molecules.

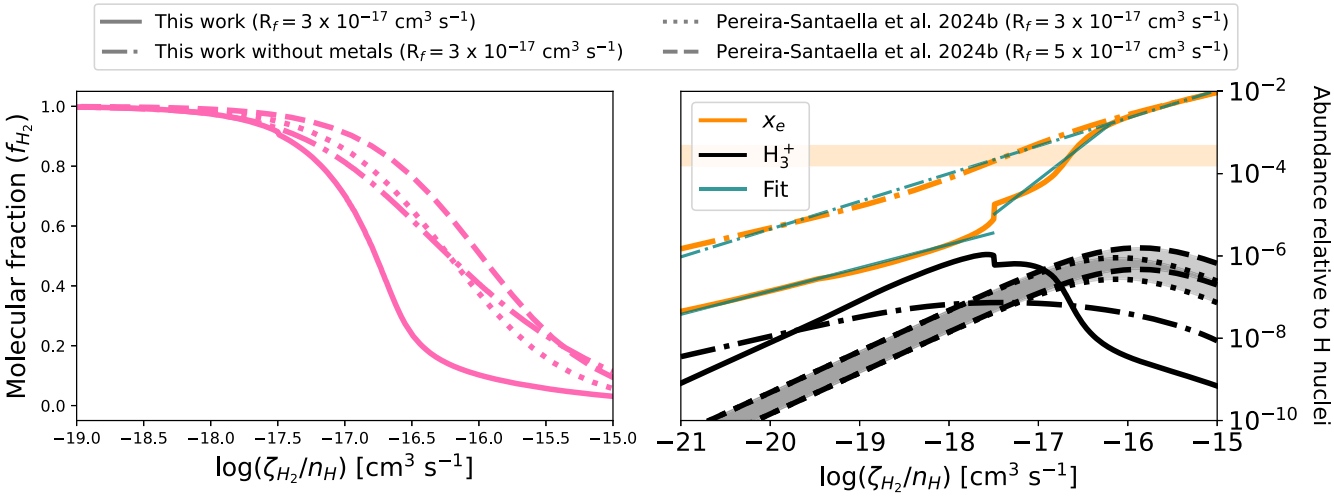

Figure E1. Comparison between the molecular fraction, $f_{H_2} = 2N(H_2)/(2N(H_2) + N(H))$, (left panel) and the fractional abundances (right panel) predicted by our chemical model for obscured dense molecular clouds and those from Pereira-Santaella et al. (2024a) for diffuse and translucent clouds. In both panels, the solid lines correspond to the model shown in Fig. 2, while the dash-dotted lines show the predictions obtained when metals are excluded from the chemical network. The dashed curve correspond to the predictions from Pereira-Santaella et al. (2024b), with $R_f = 5\times10^{-17}$ cm^3 s^{-1}. The dotted lines represent analytical predictions using the same formulation but with $R_f = 3\times10^{-17}$ cm^3 s^{-1}. In the right panel, electron and H_3^+ fractional abundances are shown in orange and black, respectively. The electron abundance, x_e, range adopted by Pereira-Santaella et al. (2024b) is indicated by the shaded orange area. The green line is the best power-law fit to x_e given by equation E1 and E2.

two ranges in order to avoid the discontinuity at log $\zeta_{H_2}/n_H \sim -17.5$.

$$\log(x_e) = \begin{cases} 0.56\log(\zeta_{H_2}/n_H) + 4.46 & \text{for } -21 < \log\zeta_{H_2}/n_H < -17.5 \\ 1.68\log(\zeta_{H_2}/n_H) + 24.52 & \text{for } -17.5 < \log\zeta_{H_2}/n_H < -16.2. \end{cases} \quad \text{(E2)}$$

For higher ζ_{H_2}/n_H, x_e from the two models overlaps.

In conclusion, the differences between our predictions and those of Pereira-Santaella et al. (2024b) arise from their model assumptions for diffuse and translucent clouds. Specifically, neglecting the role of metals and assuming a constant range of x_e can result in higher ζ_{H_2}/n_H estimates.

This paper has been typeset from a TEX/LATEX file prepared by the author.